Materials Advances

ROYAL SOCIETY OF CHEMISTRY

PAPER

View Article Online
View Journal

Cite this: DOI: 10.1039/d5ma01315a

Capturing sulfur: a comparative study on sulfur infiltration techniques of carbon aerogels and novel methods for microstructural analysis

Marina Schwan, *[a] Jessica Kröner,[a] Henrike Niehoff,[b] Peter Wagner[b] and Barbara Milow [a]

Received 12th November 2025,
Accepted 25th March 2026

DOI: 10.1039/d5ma01315a

rsc.li/materials-advances

Sulfur-infiltrated microporous carbon aerogels are widely used in metal-sulfur batteries or as a capture material for gas-phase mercury adsorption. The present paper deals with two sulfur infiltration techniques and novel characterization methods of sulfur–carbon composites. It is shown that gas-phase as well as microwave-based infiltration techniques are suitable for successful infiltration of microporous aerogels. Nevertheless, some limitations of both methods were identified. Hence, the microstructure, chemical composition, and electrical conductivity of produced samples are comprehensively analyzed. In general, sulfur was found to be partially chemically bonded with carbon, which correlates with the increase of electrical conductivity after gas-phase sulfur infiltration. Furthermore, μ-CT and electron microscopy give a very valuable insight into the structure on macroscopic level. The study provides reliable methods for detailed characterization of sulfur–carbon composites and a better understanding of sulfur infiltration techniques.

Introduction

Aerogels are highly open-porous solid materials. Carbon aerogels (CA) and their organic precursors represent a large and important class of aerogels. Their structural properties (*e.g.* porosity, pore sizes and volume, inner surface area) can be tailored for different kinds of application, such as electrode materials in rechargeable batteries or in supercapacitors,[1,2] as adsorbers for hydrogen storage[3] or catalyst support,[4] and for thermal insulation.[5]

Sulfur-infiltrated carbon aerogels have attracted a great attention in recent decades.[6–8] Several application fields have been identified for these materials.

In lithium–sulfur cells, with high theoretical gravimetric energy density of about 2.500 Wh kg^{-1} and high theoretical capacity of about 3.862 mAh g^{-1} the interest is growing in the last decades.[9] Despite other challenges, the insulating nature of sulfur, the partly irreversible relocation of polysulfides during charging/discharging and volume change of sulfur cathode belong to bottlenecks of Li–S chemistry.[10] A recent study on applying highly microporous carbon aerogels as a conductive host for sulfur was investigated.[1] The work of Nojabaee *et al.* shows crucial influence of the sulfur infiltration technique on the capacity and stability (1.050 mAh g^{-1} after 100 cycles) of the cell.

In addition, sulfur-infiltrated activated carbon is an important material for gas-phase mercury capture. The biggest source of mercury emissions is still coal fired power plant. In order to control and to decrease the release of gas-phase mercury to the environment sulfurized activated carbon was found to have a great adsorptive capacity.[11] Lui *et al.* postulated that sulfur allotropes have more active terminal atoms at higher temperatures and would facilitate more effective mercury uptake.[12] The impregnation temperature and strong bonding between sulfur and carbon essentially contribute to an excellent mercury removal.

Moreover, slow and controlled release of fertilizers or fungicides can be achieved with sulfur-containing materials.[13] Sulfur is one of the important elements for plant growth[14] and in the control against fungal diseases. Suitable infiltration techniques of carbon host would enable sustained release and long-term protection of plants.

In order to create a sulfur–carbon composite, several methods can be found in the literature.[15] The most known and applied techniques for sulfur infiltrations, based on physi- and partly chemisorption, are: (a) mill infiltration, which takes place at room temperature in a planetary ball mill, where sulfur and carbon material are placed and mixed together;[16] (b) melt infiltration conducted over several hours at temperatures

[a] Institute for Frontier Materials on Earth and in Space, German Aerospace Center (DLR), Linder Hoehe, 51147 Cologne, Germany. E-mail: Marina.Schwan@dlr.de
[b] Institute of Engineering Thermodynamics, German Aerospace Center (DLR), Carl von Ossietzky Str. 15, 26129 Oldenburg, Germany

between 155 °C and 280 °C, this method utilizes the low viscosity of liquid sulfur, allowing it to diffuse into the pores of the carbon material;[17,18] (c) vapor phase infiltration requires temperatures higher than the boiling point of sulfur (445 °C). Here, short sulfur allotropes (S_{2-4}) are present. These small molecules can diffuse into micropores (pores < 2 nm) and form covalent bonds with the carbon;[12] (d) incorporation of sulfur solved in supercritical carbon dioxide;[19] (e) solution infiltration of sulfur. In this approach, sulfur is dissolved in an unpolar solvent (*e.g.* DMSO[20,21]) and mixed with carbon material. After several hours of stirring the solvent must be removed and the composite is dried;[22] (f) microwave induced infiltration can be used to distribute sulfur within a carbon network. The carbon material acts as a microwave absorber, which melts the sulfur and facilitates its diffusion into pores of carbon matrix.[23,24]

Suitable physicochemical methods are required to analyze the sulfur infiltrated samples. Beside of TGA, DSC, XPS, and electron microscopy, μ-CT is a powerful tool for 3D analyses. It can be used to analyze all kinds of materials non-destructive in 3D as long as the X-ray can penetrate through the material. Advanced image processing can result in binarized images for further analysis to receive structural information as for example pore structures and constitution. This method finds widespread application from medical to material science for the examination of internal structures, the detection of defects and cracks of devices as well as artifacts. In energy research, this method can be used to investigate components of batteries and fuel cells on the micrometer scale.[25–38]

Despite numerous studies on melt and ball-mill infiltration techniques, the investigations on gas-phase and microwave sulfur infiltrations are incomplete. Especially, the investigations of electrical conductivity and 3D analysis are scarce and unsystematic. This work focusses on comparison of two different sulfur infiltration techniques and novel methods for microstructural analysis of carbon–sulfur composites. The drawbacks and benefits of sulfur-infiltration methods are discussed by applying different characterization techniques to obtain a comprehensive understanding. In this study, the sulfur distribution within the porous network and the efficiency of both techniques are investigated as key parameters. Given that the filling of micropores with sulfur is crucial for various applications, this aspect was analyzed in detail *via* TG analysis.

Synthesis and methods

Classification of aerogels

For this study, two types of carbon aerogels (CA) were produced. Both types of CA are based on a flexible resorcinol-formaldehyde (RF) aerogel.[39] The first type, an activated CA, is termed CA_a. The second type is activated and nitrogen-doped and is termed CA_{ad}.

The CAs were infiltrated with sulfur both in gas phase CA_a–S_{Gas} and CA_{ad}–S_{Gas}, respectively, and in microwave CA_a–S_{MW} and CA_{ad}–S_{MW}, respectively.

Synthesis of resorcinol-formaldehyde (RF) aerogels

Resorcinol (R) (98%, Aldrich) was dissolved in deionized water (W) at a molar ratio R:W of 0.008 at room temperature and stirred with a cross-magnetic stir bar at 150 rpm. Then an aqueous solution of formaldehyde (F) (37% w/w, stabilized with 10% methanol, Merck) and solid sodium carbonate (C) (Aldrich) was added to the stirred resorcinol solution. The R:C and R:F molar ratios were 50 and 0.5, respectively. The pH was adjusted to 5.4–5.6 after stirring for 5 minutes by dropwise addition of 2 N nitric acid (Alfa Aesar). Stirring at room temperature was continued for 60 min, followed by placing the homogeneous, transparent solution in a sealable polypropylene container in an oven at 60 °C (Memmert GmbH, Germany). After 7 days of gelation, the wet gel was cooled to room temperature and transferred to an acetone bath (pure, technical grade, TH. Geyer) to remove the remaining chemicals and exchange water with acetone, which is soluble in supercritical carbon dioxide. The acetone was refreshed six times within 3 days. Supercritical drying was carried out with CO_2 (purity ≥99.995%, Praxair) in an autoclave of 60 L volume (Eurotechnica, Germany) at 60 °C and 110 bar for about 21 h in total. The total duration is made up of three main steps: System start-up (2–3 h), solvent extraction (5–6 h), depressurization and system shutdown (2–3 h), overnight the system was kept at constant pressure and temperature. The degassing was carried out in an autoclave of 60 L volume (Eurotechnica, Germany). The degassing rate was set to 0.2 bar per minute.

Synthesis of CA_a: carbonization and activation

The carbonization was carried out in an electric furnace (KS-3-80-Vac-Sonder, Linn High Therm, Germany) using nitrogen (purity ≥99.999, Linde). The RF aerogel was placed in the furnace, purged three times with nitrogen, and heated to the carbonization temperature of 800 °C. The heating rate was adjusted to 5 K min^{-1}, and the pressure was adjusted to 50 mbar. The temperature was kept for 5 h. Subsequently the activation was performed using CO_2 with a flow of 9 L h^{-1} at 1000 °C for 3 h. After carbonization and activation, the aerogels were cooled down to room temperature under a flow of nitrogen.

Synthesis of CA_{ad}: nitrogen doping and activation

RF aerogel was placed with melamine (99%, Alfa Aesar) and potassium carbonate (99.5%, Merck, Germany) in a weight ratio of 1 : 1 : 1 in a shaker ball mill (MM400, Retsch GmbH, Germany). After milling for 30 s with 30 Hz and three balls (stainless steel, ∅ = 15 mm), the mixture was carbonized in an electric furnace (KS-3-80-Vac-Sonder, Linn High Therm, Germany) using nitrogen (purity ≥99.999, Linde). The sample was purged three times with nitrogen, and heated to the carbonization temperature of 800 °C. The heating rate was adjusted to 5 K min^{-1}, and the pressure was adjusted to 50 mbar. The temperature was kept for one hour whereupon the samples were cooled down to room temperature under a flow of nitrogen.

After carbonization the samples were washed with deionized water until a neutral pH value of the solvent was reached, to remove the K_2O. After washing, the samples were dried at a temperature of 50 °C for 24 h.

Gas phase sulfur infiltration

For the gas infiltration the carbon aerogel and the glass flask were heated at 100 °C under vacuum for 12 h. Afterwards the CA and the sulfur powder (99.5%, Alfa Aesar, Germany) are milled in a shaker ball mill (MM400, Retsch GmbH, Germany) under argon atmosphere (purity ≥99 999%, Linde) for 30 s and 30 Hz with 3 milling balls (∅ = 15 mm). Further the sample was filled in a glass flask under argon conditions. After evacuation the ampulla was sealed under vacuum. The maximum sulfur vapor pressure p_{max} at the temperature (T) 600 °C was calculated using eqn (1). To avoid damage to the glass ampulla with volume $V_{ampulla}$ and the subsequent release of hazardous sulfur oxides into the environment, the wall thickness of ampulla was adjusted accordingly. The sulfur amount $m_{S,max}$ was calculated from the micropore volume of the CA (eqn (4)) and M(S) molar mass of sulfur. A closed system was generated which was treated at 600 °C for 6 h in an electric furnace (KS-3-80-Vac-Sonder, Linn High Therm, Germany). After heat treatment the temperature was decreased slowly.

$$m_{S,\,max} = \frac{p_{max} \cdot V_{ampulla} \cdot M(S)}{R \times T} \quad (1)$$

Microwave sulfur infiltration

For the microwave infiltration the carbon aerogel and the microwave tube were heated at 100 °C under vacuum for 12 h. Afterwards the CA and the sulfur powder (99.5%, Alfa Aesar, Germany) are milled in a shaker ball mill (MM400, Retsch GmbH, Germany) under argon atmosphere (purity ≥99 999%, Linde) for 30 s and 30 Hz with 3 milling balls (∅ = 15 mm). The sulfur amount was calculated from the micropore volume of the CA (eqn (4)). Further the sample was filled in the microwave tube under argon conditions and sealed. The tubes were placed central so that continuous, unpulsed microwave radiation is focused on the reactor (wavelength 12.2 cm) and were heated up to 250 degrees at 300 W in the microwave (Discover, CEM, Germany). The microwave treatment was 5 minutes. The non-contact temperature sensor located underneath the container measures the temperature development in the pressurized container. The frequency is not user-adjustable, the single-mode microwave technology is used in the device. After heat treatment the temperature was decreased.

Characterization techniques

For physisorption experiments the samples were degassed for 12 h at 200 °C and 0.1–0.5 mbar (SmartVacPrep, Micromeritics, Germany). The measurement of specific surface area, meso- and micropore size distribution, mesopore volume, and micropore volume were performed at 77 K by nitrogen adsorption–desorption isotherms (3Flex, Micromeritics, Germany). The calculations were based on BET/BJH/DFT/t-plot methods. For t-plot and BJH, a Carbon Black STSA model and for DFT method, a classical N2@77 carbon model for slit pores was used. Additionally, micro pore distribution was measured at 273 K with carbon dioxide (TriStar, Micromeritics, Germany). The calculation is based on classical CO_2-DFT-Model for slit pores

The electrical conductivities were measured using a powder resistivity measurement system based on a DC voltage-current measurement (PD-51, Mitsubishi Chemical Europe). The measurement was based on a 4-pin method at different pressures. The thickness of the sample was determined using a displacement transducer.

The microstructure of carbon aerogels was investigated using Raman spectroscopy (XploRA PLUS, Horiba Scientific, Germany) using a laser wave length of 532 nm. For each spectra the acquisition time was adjusted to 60 s. The ratio I_D/I_G was calculated from the intensities of the D and G peaks.

The elemental (CHNS) analysis was done with an EA300 from EuroVector®. For the elemental analysis the compounds were brayed with vanadium (V) oxide and burned at 1000 °C with a subsequent gas chromatography.

Thermogravimetric analysis was performed under an argon atmosphere using an STA 449 F3 Jupiter (Netzsch, Germany). The heating rate was adjusted to 10 K min^{-1}, the temperature range was 22 °C to 1000 °C. The average sample mass was 2.45 mg.

ATR-FTIR spectroscopy was performed on a Tensor 27 spectrometer (Bruker Optics GmbH & Co. KG, Germany) measuring a total of 150 scans over a spectral range of 4000–400 cm^{-1} with a resolution of 4 cm^{-1}, for each sample. In total, three spectra for each sample were averaged and analyzed.

X-ray photoelectron spectroscopy (XPS) was performed using VersaProbeII instrument (Ulvac-Phi). The samples were irradiated with an aluminum Al-Kα emitter with an energy of $h\nu$ = 1486.6 eV in a spot diameter of 100 μm. Detection was carried out with a hemispherical analyzer. To ensure charge compensation during measurement, a dual-beam system consisting of an electron shower by a Flood-Gun and low-energy Ar^+ ions was used simultaneously. The pass energy was set to 11 eV. The acquisition time for the S 2p spectra was 19 minutes and 30 seconds. For peak fitting of the S 2p region, the full width at half maximum (FWHM) was constrained to 0.8–1 eV for S–Cx and 1.5–2.4 eV for C–SOx.

The 3D visualization of the powder samples was achieved by X-ray μ-computed tomography (μ-CT). Therefore, a small amount of CA powder was put in a home-made cylindrical plastic holder (*ca.* 6 mm diameter) and covered with parafilm. The measurements were performed with a Skyscan 1172 device by Bruker (Belgium). The X-ray source was set to maximum power of 80 kV and 0.1 mA and the images were recorded in a step size of 0.2° with an exposure time of 1425 ms. Frame averaging was set to 4 and random movement to 10. A resolution of 2–4 μm per pxl was achieved. The reconstruction of the single images into a 3D volume stack was achieved using the software NRecon (Bruker, Belgium) for which the image

greyscales had to be adjusted partly individual due to different densities of the CAs. Cross-sections and 3D images were received using the software DataViewer and CT_{Vox}, respectively (both Bruker, Belgium).

Scanning electron microscopy (SEM) coupled with energy dispersive spectroscopy (EDS) was performed on a Hitachi S-3200N microscope and an Oxford INCA System with PentaFET Precision INCA X-Act (10 mm^2 SDD detector). The powder samples were attached to a carbon tape on an aluminum sample holder. Several different sample spots (3–4) on the holder and different magnifications were analyzed. Most representative images are selected.

High-resolution transmission electron microscopy (HR-TEM) was performed on a Jeol JEM2100 F microscope using a Schottky emitter as electron source, acceleration voltage of 200 kV and magnification up to 1 000 000. The samples were analyzed on a Cu grid covered polyvinyl formal film (200 mesh, Plano). For TEM analysis, overview images were taken first. In case of promising results (stable sample on the holder, not too much sample in one region) high-resolution TEM images were acquired.

Results and discussion

First, the morphology, chemical structure, and physical properties of two pure carbon aerogels and aerogels doped with nitrogen are discussed. This is followed by discussions of different infiltration techniques and their influence on the sulfur loading and distribution within carbon network.

Table 1 and Fig. 1 summarize the properties of carbon aerogels. The SEM images (Fig. 1a and b) depict the morphology of both carbon aerogels. The backbone of both aerogels consists of interconnected, quasi-spherical nanoparticles. These particles are covalently bonded to one another, forming a continuous, branched skeletal structure. This connectivity ensures high electrical conductivity and mechanical stability. The spaces between the particle chains create a complex system of pores. Large pores between big clusters can be observed from SEM images, which are not detectable with gas sorption techniques. The particle size estimated from scanning electron microscopy is in the range of 150 ± 50 nm.

To evaluate the surface area and the pore size distributions gas sorption was used. Specific surface areas were derived from the N_2 adsorption isotherms based on the BET model. The linear fit was restricted to the relative pressure range of p/p^0 = 0.05 to 0.2 to ensure a positive C constant and to satisfy the Rouquerol criteria. The regression resulted in an R^2 value of about 0.999, confirming the validity of the multipoint fit. The linear fit, correlation coefficient R^2 as well as BET C constant are present in SI (Fig. S1a and Table S1). Both aerogels CA_a and CA_{ad} have type I(a) isotherm provided by microporous solids which is confirmed by a steep increase of N_2 uptake at low p/p^0 value with small contribution from Type IV behavior (Fig. 1c). The nitrogen uptake of CA_{ad} is distinctly much higher than CA_a, indicating higher micropore volume. A plateau appears in the relative pressure range between $0.1 < p/p^0 < 0.8$ with a small increase of gas uptake at high $p/p^0 > 0.9$ originated from small ratio of mesopores ($V_{meso}CA_a$ = 0.09 $cm^3\ g^{-1}$ and $V_{meso}CA_{ad}$ = 0.16 $cm^3\ g^{-1}$). Fig. 1e shows the pore size distributions of aerogels calculated from nitrogen sorption measurements. Both aerogels reveal a bimodal pore size distribution. CA_a shows a sharp peak at around 0.64 nm and a second small peak at 1.27 nm. Whereas, CA_{ad} has two very broad peaks: double-peak at 0.68 and 0.90 nm and at around 2.5 nm. Additionally, CA_{ad} exhibits considerably larger surface area and almost three times higher micropore volume. For further analysis of the micropores, CO_2 sorption measurements were conducted at 273 K. The samples exhibit Type I isotherm which is characteristic of microporous solids (Fig. 1d). Notably, significant discrepancies between the results from the nitrogen adsorption and those obtained from the CO_2 adsorption were found for the nitrogen-doped sample CA_{ad}. The N_2 isotherm of CA_{ad} shows a distinctly higher micropore volume and nitrogen uptake compared to CA_a whereas, the apparent CO_2 uptake on CA_{ad} is lower than on its non-doped counterpart.

To elucidate the mechanisms underlying these differences the pore size distributions of both materials were examinate. The analysis of the obtained results shows a bimodal shape for the pore size distributions (Fig. 1f) with pores between 0.4 and 1.1 nm. For CA_a, a primary peak with significantly high intensity appears at about 0.55 nm, followed by a secondary peak of lower intensity at about 0.85 nm. Conversely, the first peak for CA_{ad} is right-shifted to 0.59 nm, while its second peak – exhibiting higher intensity - is centered at 0.85 nm.

In summary, CA_a has a lower total micropore volume, but a higher pore volume in the sub- 0.6 nm range. In contrast, the total micropore volume of CA_{ad} is three times higher, but its pores are predominantly situated in the region above 0.8 nm. The picture that emerges from considering of the micropores, CO_2 uptake and micropore volume for CA_a are higher for the region below 0.6 nm; meanwhile, the larger micropores (>0.8 nm) in CA_{ad} remain undetected by CO_2 measurements, as CO_2 adsorption is typically restricted to pores smaller than

Table 1 Microstructural and compositional properties of pure carbon aerogels

	V_{micro} [$cm^3\ g^{-1}$]	V_{meso} [$cm^3\ g^{-1}$]	A_{BET} [$m^2\ g^{-1}$]	Conductivity at 3.18 MPa [$S\ m^{-1}$]	C [wt%]	H [wt%]	O [wt%]	N [wt%]	I_D/I_G
CA_a	0.30 ± 0.02	0.09 ± 0.0	828 ± 21.5	234 ± 21.5	88.3 ± 1.70	0.77 ± 0.63	3.34 ± 1.21	n.d.[a]	1.35 ± 0.03
CA_{ad}	1.02 ± 0.08	0.16 ± 0.04	2440 ± 110	417 ± 24.2	77.5 ± 0.21	n.d.[a]	3.36 ± 0.04	1.28 ± 0.14	1.39 ± 0.05

[a] n.d.: not detected.

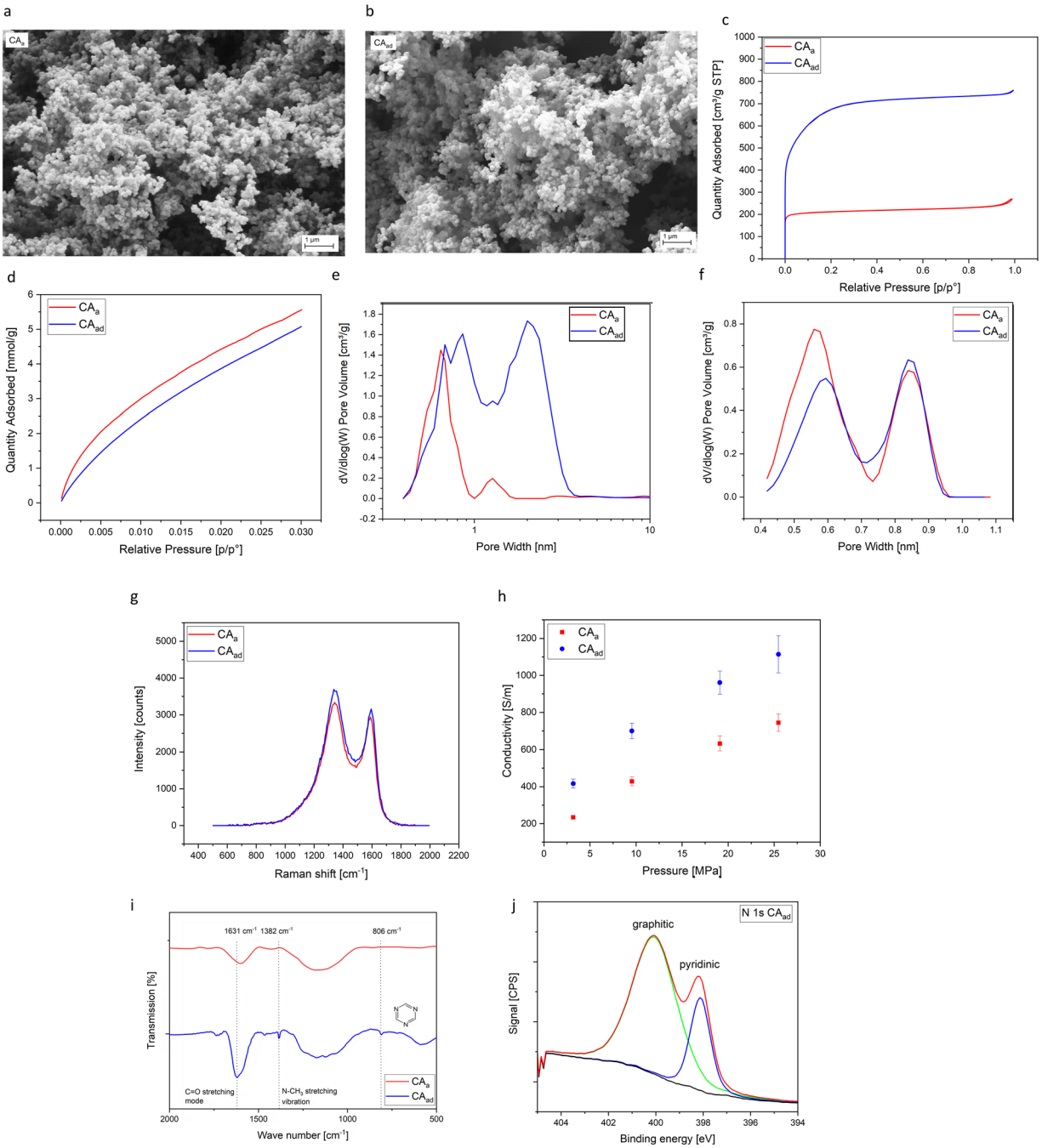

Fig. 1 (a) SEM images of microstructure of CAa and (b) of CAad aerogels; (c) nitrogen adsorption–desorption and (d) CO_2 adsorption isotherms; (e) pore size distributions from nitrogen sorption at 77 K and (f) and from CO_2 gas sorption at 273 K of carbon aerogels; (g) Raman spectra of carbon aerogels; (h) electrical conductivity of pulverized carbon aerogels under pressure; (i) IR-spectra of activated CA_a and N-doped carbon CA_{ad} aerogels; (j) N 1s spectrum of N-doped carbon aerogel CA_{ad}.

0.8 nm.[40] Consequently, the results from carbon dioxide and nitrogen sorption measurements complement each other well.

Furthermore, the role of nitrogen doping must be considered because the molecular polarity of CO_2 is larger than that of N_2, an adsorbent with a polar surface (*e.g.* a nitrogen-doped material) may increase the adsorption difference between the two gases. CO_2 molecules and the adsorbent can form strong interaction energies in the narrow pores. However, in our case, it appears that the CO_2 adsorption is not influenced by relatively low nitrogen content, but rather by the pore architecture.

The structural changes are associated to both, CO_2 activation and the reduction of K_2CO_3 according to the reactions:[41]

$$K_2CO_3 \rightarrow K_2O + CO_2 \quad (2)$$

$$CO_2 + C \rightarrow 2CO \quad (3)$$

In CA_{ad} high amount of carbon is removed as CO gas causing creating of high surface area, and high micropore volume of 1.02 $cm^3\ g^{-1}$. Whereas, the activation with CO_2 leads to 0.30 $cm^3\ g^{-1}$ micropore volume. Moreover, Sevilla *et al.* figured out a crucial role of melamine during activation process.[42] The presence of melamine for CA_{ad} not only leads to nitrogen doping (1.28 wt%), it also contributes to the development of porosity. The increase of pore volume can be attributed to the formation of carbon nitride and its gradual decomposition at around 400 °C, which causes development of porosity and widening of pores. The chemical composition of synthesized samples was studied by elemental analysis. In CA_a low amount of hydrogen and oxygen can be identified. CA_{ad} exhibits similar amount of oxygen and, since it was doped with melamine, also nitrogen could be proven.

The structural properties of carbon aerogels were further analyzed with Raman spectroscopy. Fig. 1g reperesnts Raman shift of the amorphous and graphitized regions of both aerogels and an example of the evalution is presented in SI (Fig. S1b). The spectra exhibit two bands at around 1340 and 1590 cm^{-1} responsible for the D and G bands, respectively. The D band at around 1340 cm^{-1} is associated to the breathing mode of sp^2 carbon present in the 6-membered aromatic rings with defects. The G band with lower intensity at around 1590 cm^{-1} is caused by the bond stretching motion of the sp^2 hybridized carbon atoms in the graphitic structure. The I_D/I_G ratio for both types of aerogels are presented in Table 1. Higher I_D/I_G ratios are typical for disordered carbon materials like amorphous carbon with high concentration of defects. It is tremendously evident from high I_D/I_G ratio that both materilas have in their structures defects and disorder. The I_D/I_G ratios are close to each other. Nevertheless, the CA_{ad} shows higher degree of disorder with I_D/I_G of 1.39. The catalytic action of Potassium hinders the long-range ordering (graphitization) of the carbon, favoring the formation of amorphous, disorganized structures. Furthermore, at temperatures above 800 °C K_2CO_3 produces metallic K, which intercalates into the graphitic lattice. This intercalation causes expansion and structural disruption of the ordered carbon sheets.

Fig. 1h shows the electrical conductivity of carbon aerogels CA_a and CA_{ad} at different pressures. With increased pressure the conductivity rises, due to densification of powder and creating of new pathways for electron transfer. The electrical conductivity of nitrogen doped carbon aerogel CA_{ad} is almost twice as high at 3.18 MPa as the non-doped aerogel. The doping process seems to have a great influence on the electrical conductivity. This could be attributed to changes in the microstructure during activation with potassium carbonate, to doping with melamine, and to the presence of nitrogen. In general, N-atoms can be integrated into carbon aerogels as structural (pyridinic, pyrolic, and graphitic) or as chemical (nitro- or amine-groups) nitrogen. The structural nitrogen substitutes carbon atoms and contributes to p-electrons to the π-conjugated system. Caused by the larger electronegativity of nitrogen (3.0) compared to carbon (2.5) the electrical conductivity of nitrogen-doped material increases which is observed by several studies.[43,44] The incorporated nitrogen was studied by IR and XPS spectroscopies. Fig. 1i shows IR spectra of both carbon aerogels. A peak at around 1630 cm^{-1} can be identified for both materials which is related to stretching region of C=O bonds.[45] Moreover, additional peaks of stretching modes of $N–CH_3$, as well as nitrogen from triazine rings can be seen in CA_{ad}. The N 1s spectrum in Fig. 1j is used to analyze the nature of nitrogen functionalities. The N 1s spectrum can be deconvoluted into two peaks at 400.1 and 398.1 eV, corresponding to graphitic and pyridinic bonded nitrogen, respectively. Both, graphitic and pyridinic nitrogen influence the overall electrical conductivity,[46] which is in agreement with our investigations. Both analytical methods show successful doping of nitrogen by adding of solid melamine and subsequent increase of electrical conductivity.

For this work, two sulfur infiltration techniques suitable for porous carbon materials were elected.

Fig. 2c schematically illustrates both techniques. The vapor phase infiltration technique is very advantageous for several applications due to small sulfur molecules present in the gas phase. Generally, the equilibrium vapor of sulfur at about 450 °C contains all molecules S_n ($2 < n < 10$), but the S_2 molecules are in the majority.[47] These molecules have a cross-sectional diameter of 3.7 Å[48] and can strongly interact with the inner surface of carbon matrix (*e.g.* pore walls) and fill first the micropores and then create monolayers.[49] Important is to point out, that after cooling to room temperature sulfur inside the micropores remains as the state of S_2.[50]

The sulfur infiltration by use of microwaves also seems to be suitable for micropores carbon materials. The infiltration was carried out at 250 °C. Although, the direct temperature measurement during microwave treatment remains a challenge due to hotspots caused by the absorption of carbon-based materials and the requirements for safe containment of the microwave reactor, for the discussion of results adjusted temperature (250 °C) is used. Microwaves are high-frequency electromagnetic waves with a frequency between 300 MHz and 300 GHz.[51] Because of the much lower frequency, microwaves carry less energy compared to X-rays or γ-rays and thus, have only a thermal effect on materials. Sulfur has a high transparency to microwaves and can be heated up only mixed with a microwave receptor. In this study, carbon aerogels act as a microwave active material. As suggested by Kim *et al.*, the active carbon atoms are induced to dipole moments by the electromagnetic field of the microwaves.[52] The charge-bearing atoms try to align themselves in the direction of the permanently changing electromagnetic field, and the material-related damping of the oscillations leads to a time delay. This results in a heat loss. Due to the carbon atomic structure, activated carbon material has free electrons, which is why electric currents can be induced by microwaves. This results in heating of the activated carbon due to inductive heat. From heated carbon the energy is translated to the sulfur and causes melting or even evaporation of it, as reported by Dubey and Dube,[53] recently.

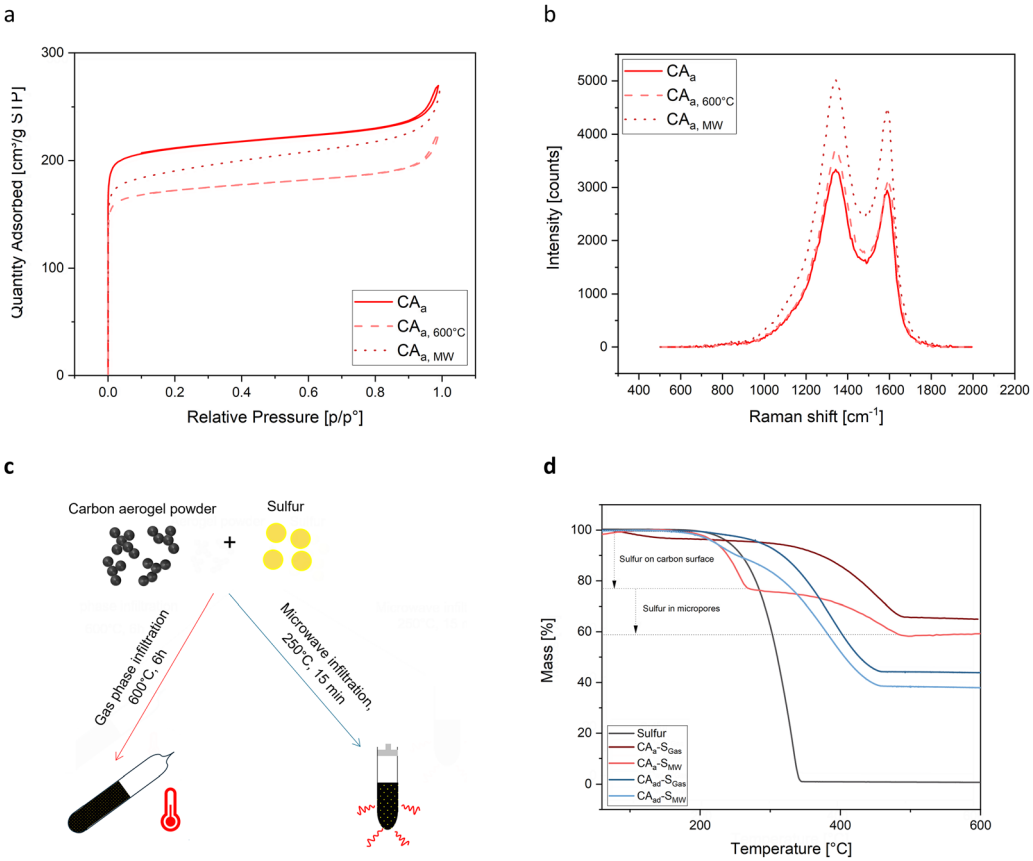

Fig. 2 (a) Pore size distribution of untreated CA_a and after heat treatment at 600 °C and microwave treatment; (b) Raman spectra of untreated CA_a and after heat treatment at 600 °C and microwave treatment; (c) schematic illustration of infiltration techniques and process parameter; (d) TGA curves of sulfur and sulfur-infiltrated carbon aerogels showing two main steps of sulfur loading on the external surface and in the micropores.

In order to disentangle sulfur-specific effects from microwave- or heat-induced alterations of the carbon framework, activated carbon aerogel CA_a was subjected to identical microwave $CA_{a,\ MW}$ and gas-phase CA_a, 600 °C conditions without sulfur. The results are shown in Fig. 2a and b and in Table 2.

To evaluate the changes in the specific surface area and pore sizes (Fig. S2) N_2 gas sorption measurements were performed. The surface area of CA_a, 600 °C is 10% and CA_a, MW 8% lower compared to the untreated sample CA_a. It can be considered that long heat treatment at 600 °C led to structural changes. At temperatures above 500 °C the carbon structure undergoes annealing and consolidation, causing closing of pores, shrinking, or even sintering processes. The results from Raman measurements show that I_D/I_G value decreases indicating higher degree of order. The long heat treatment enhances the alignment of graphitic crystallites, reducing the interlayer spacing and decreasing the overall pore volume.

In contrast, the microwave treatment causes higher degree of disorder in carbon aerogel (I_D/I_G = 1.42). This is due to rapid, non-uniform heating, local hot spots, and non-thermal effects that disrupt existing crystalline structures, causing structural rearrangements or defects, rather than the gradual ordering seen in thermal treatment at 600 °C. These findings are in agreement with Deng *et al.*[54]

Sulfur loading in carbon aerogels was analyzed thermogravimetrically. TGA measurements, shown in Fig. 2d, indicate the sulfur loading in the carbon aerogels. In general, TGA-curves of samples infiltrated in the gas-phase have a different course compared to microwave. Gas-phase infiltrated samples reveal a flat curve up to about 280–320 °C and then the mass drops down, from about 480 °C they flatten out. For microwave-infiltrated samples, the curves show two steps: at 180–240 °C and at 280 °C. A mass reduction between 180 °C and 230 °C is attributed to the evaporation of surface sulfur (sulfur placed on the external surface of carbon network) and sulfur in mesopores. The evaporation of sulfur trapped in the micropores requires additional energy, resulting in mass loss at higher temperatures at 250 °C to 450 °C. Similar observations were made by Tang *et al.*[55] In this study, mass loss of sulfur confined

Table 2 Microstructural and compositional properties of pure untreated and treated carbon aerogels

	V_{micro} [$cm^3\ g^{-1}$]	V_{meso} [$cm^3\ g^{-1}$]	A_{BET} [$m^2\ g^{-1}$]	I_D/I_G
CA_a	0.30 ± 0.02	0.09 ± 0.00	828 ± 21.5	1.35 ± 0.03
CA_a, 600 °C	0.27 ± 0.02	0.10 ± 0.02	740 ± 64	1.30 ± 0.06
CA_a, MW	0.26 ± 0.00	0.13 ± 0.01	761 ± 17	1.42 ± 0.02

Table 3 Theoretical and experimental sulfur loading in micropores and on carbon surface (Rev1, com. 4)

Sample names	Experimental sulfur loading, [wt%]			Theoretical sulfur loading in micropores w_S, [wt%]	Infiltration efficiency, [%]
	Total	On carbon surface	In micropores		
CA_a-Gas	31.8 ± 2.2	0.0	31.8 ± 2.2	34.7	93.5
CA_a-MW	41.2 ± 1.4	23.0 ± 1.6	18.2 ± 1.2	34.7	53.5
CA_{ad}-Gas	55.5 ± 3.8	0.0	55.5 ± 3.8	63.8	88.1
CA_{ad}-MW	61.2 ± 2.1	10.1 ± 0.7	51.1 ± 3.5	63.8	81.1

in the microporous of carbon was observed at 300 °C. All gas phase infiltrated curves show that the sulfur is present predominantly in the micropores. Due to the higher micropore volume of CA_{ad}, a higher mass loss occurs in the aerogel. Table 3 summarizes theoretical and experimental sulfur loading. The theoretical sulfur loading $w(S)$ was calculated with[56]

$$w(S) = \frac{V_{micro} \times \rho_S \times m_{CA}}{V_{micro} \times \rho_S \times m_{CA} + m_{CA}} \times 100 + 10\% \quad (4)$$

The eqn (4) from Usuki *et al.* was adapted, additionally to micropore volume V_{micro}, density of sulfur ρ_s, and mass of carbon aerogel m_{CA}, 10 wt% of sulfur were added to the theoretical sulfur amount due to mass loss during decanting, transfer and infiltration.[50]

The theoretical sulfur loading for CA_{ad} (63.8 wt%) is almost two times higher compared with CA_a (34.7 wt%) due to its higher micropore volume. From the TGA curves a predominant confinement in micropores with gas-phase infiltration can be observed. Remarkable, the mass loss for CA_{ad} starts already at about 220 °C and for CA_a at higher temperature, at 300 °C. Due to the fact that the CA_a consists predominantly of pores smaller 1 nm and CA_{ad} exhibits additional high volume of pores between 1 and 2 nm, it is expected that sulfur will evaporate first from the larger micropores and later, at higher temperatures from smaller micropores. Nevertheless, not all available micropores were filled with sulfur. The efficiency of gas-phase infiltration technique for CA_a is 93.5% and for CA_{ad} is significantly lower with 88.1%. This may be caused by undesired sulfur deposition on the walls of the glass ampoule. At higher sulfur amounts, sulfur deposition on the reactor walls also appears to be more dominant. Moreover, sulfur molecules present in the gas phase are small showing a tendency to fill ultramicropores (pores smaller 0.7 nm). Thus, pores of about 1–2 nm are not filled completely by this technique.

In contrast to the gas-phase infiltration, microwave infiltration leads to large amount of sulfur in mesopores and on the external carbon surface. For CA_a nearly a half of total sulfur amount (23.0 wt%) could be found on the surface, and only 18.2 wt% in the micropores. Therefore, the efficiency of the microwave technique for CA_a is the lowest (53.5%). For CA_{ad} a five times higher amount of sulfur (51.1 wt%) could be analyzed in the micropores. The efficiency of microwave infiltration is almost 34% higher for CA_{ad} (81.1%) compared to CA_a (53.5%). During microwave treatment sulfur molecules are much larger than in the gas-phase, so that the filling of larger pores (mesopores) predominates with this technique. Small micropores below 1 nm of CA_a remain partially inaccessible, which reduces the efficiency.

In principle, three main parameters must be taken into account when evaluating TGA: pore sizes of carbon aerogel; pore volume, and the infiltration technique. Considering these three influencing factors for the evaluation of infiltration technique, the efficiency can be summarized as follow: for carbon materials with small micropores (below 1 nm) gas-phase infiltration technique is the most suitable; for carbon materials with larger micropores (1–2 nm) and mesopores the microwave techniques is recommended. Although the micropores could be filled with both techniques, the efficiency of gas-phase infiltration technique is the highest. Considering the fact that for the desired application (Li–S battery, mercury trapping) exclusively micropores need to be infiltrated, microwave technique should be improved prior using it for those purposes.

The phase transition of sulfur was determined by use of differential scanning calorimetry (DSC). As shown in Fig. 3a, the curves of elemental sulfur and sulfur infiltrated samples differ from each other. Elemental sulfur consists of S_8 crown-shaped rings at room temperature. The DSC thermogram of elemental sulfur contains four endothermic signals. First, the melting of α-$S_8^{\bullet}$ (ortho-rhombic sulfur) takes place at 114 °C. The second peak at around 124 °C is related to the melting of the β-crystals. The λ-transition at around 168 °C is apparently visible in a DSC thermogram. At that temperature S_8 rings are broken and converted into a linear polymeric bi-radical molecules ($^{\bullet}S–S_6–S^{\bullet}$). The entropic driven forces become more dominate and the polymeric fraction of the liquid grows. Due to the formation of polymeric chains sudden and high large increase in viscosity occurs.[57] Finally, above 334 °C molten sulfur transits to the gas phase, which is characterized by a pronounced endothermic signal. Remarkable, the DSC curves of infiltrated samples have a different shape. Here, microwave infiltrated and gas infiltrated samples were analyzed as examples in order to investigate the differences caused by different infiltration methods. A broad signal between 50 °C and 100 °C appears first, followed by a second endothermic signal from 150 °C to 220 °C. The curves undoubtedly show that after infiltration no crystalline sulfur can be observed in carbon aerogels. Moreover, sulfur infiltrated CAs exhibit considerably higher evaporation temperature at around 460 °C which demonstrates formation of strong bonds between sulfur and carbon during infiltration, consistent with the XPS results. Ye *et al.* observed similar behavior of sulfur loaded carbons.[58]

Fig. 3b compares the electrical conductivity of pure and sulfur-infiltrated carbon aerogels at different pressures.

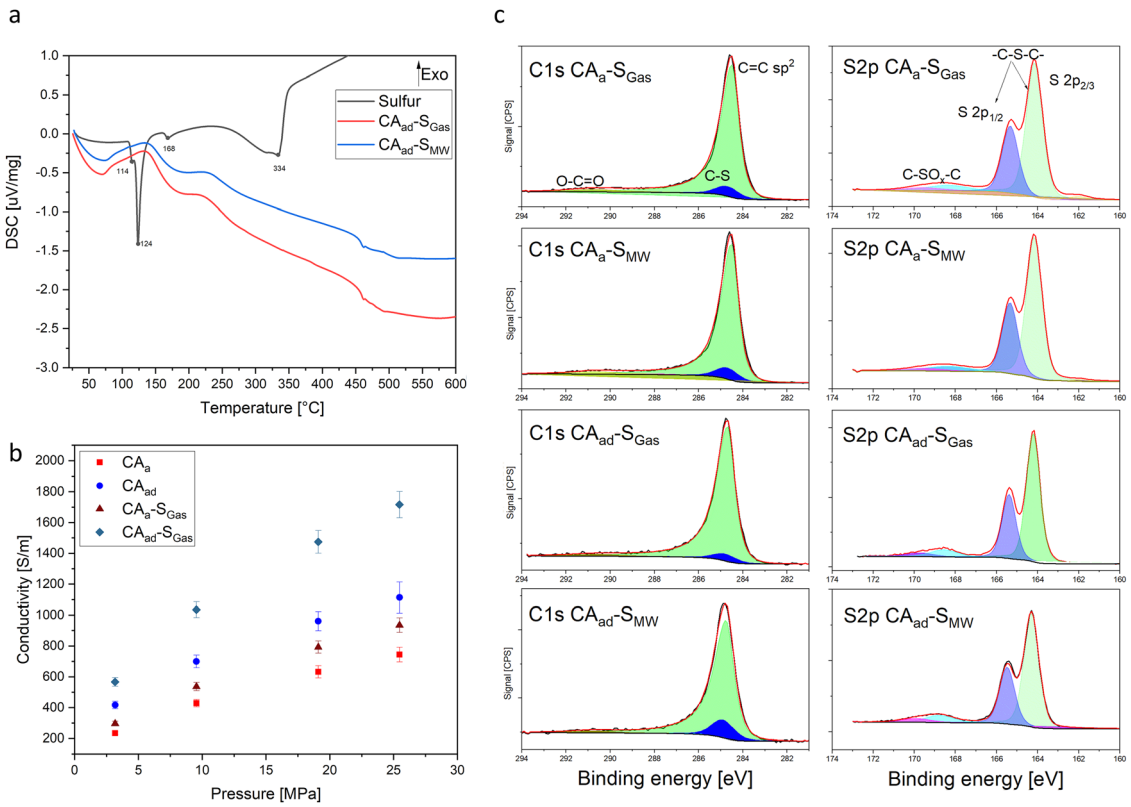

Fig. 3 (a) DSC curves of sulfur-infiltrated carbon aerogels; (b) electrical conductivity of pure and sulfur-infiltrated carbon aerogels; (c) C 1s and S 2p XPS spectra of sulfur infiltrated samples.

The infiltrated carbon aerogels exhibit higher conductivity than pure aerogels, although the sulfur has a non-conductive nature. Two different processes can contribute to the increase of electrical conductivity. On the one hand, the sulfur infiltration takes place at 600 °C and, additionally to the infiltration, cause changes in aerogel structure as already discussed and shown in Fig. 2b, *e.g.* microstructure rearrangements during heat treatment, changing in size of crystallite or appearance of defects.[59] On the other hand, sulfur is known as a highly reactive element for heteroatom doping because of its unpaired electrons and small difference in the electronegativity with carbon (electronegativity of sulfur (2.58) and carbon (2.55)).[60] Many authors have observed improved conductivity of sulfur-doped carbon materials.[61–63]

The XPS measurments were carried out to evaluate the S and C surface species. For both aerogels and both techniques the spectra appear similar Fig. 3c, although CA_{ad} is doped with nitrogen. The peak in C 1s spectrum of sp^2 carbon appears at 284.5 eV, another fitted peak of C–S bond can be seen at 284.7 eV, which further proves covalently bonded sulfur. Other broader peaks between 289 and 290.75 eV can be assigned to C–O bonds. The S 2p spectrum of both infiltrated aerogels show the typical signals for C–S bonds.[64] The S $2p_{3/2}$ signal at 164.15 eV and S $2p_{1/2}$ at 165.33 eV can be assigned to –S–C–S– covalent bond of thiophene sulfure owing to their spin–orbit coupling. Similar result was also reported by Ma *et al.*[62] SO_x species (*e.g.* sulfate –C–SO_4–C– or sulfonate –C–SO_3–C–) are observed at 168–170 eV, as proposed by Wang *et al.*[63]

The morphology of infiltrated aerogels based on CA_a appears similar as seen in the reconstructed 3D images (Fig. 4). Here, the resolution of µ-CT measurement (2–4 µm per pxl) defines the information depth of the presented images, so that the microstructures and micropores cannot be visualized as they are roughly one order of magnitude smaller. The two infiltrated CA_a samples are comparable indicating a similar structure after sulfur infiltration and no influence of the two different methods used here. The powders are relatively homogeneous with small, mostly elongated particles. Here it can be seen that the density of the majority of the powder is similar while the infiltration leads to a second phase with higher density appearing as the mentioned particles.

Sulfur infiltrated aerogels of the type CA_{ad} reveal different morphologies compared to CA_a samples. The sample from gas infiltration (CA_{ad}–S_{Gas}) seems to have an overall higher density (appears much brighter in Fig. 4c) while the aerogel from microwave infiltration CA_{ad}–S_{MW} appears very inhomogeneous with large aggregates of a material with a higher density. This could indicate a separation of sulfur particles and therefore an unsuccessful sulfur infiltration, which is in accordance with the TGA results. TGA results reveal a high sulfur loading for the microwave infiltrated samples compared to the ones from gas phase infiltration. The highest sulfur content was found for the

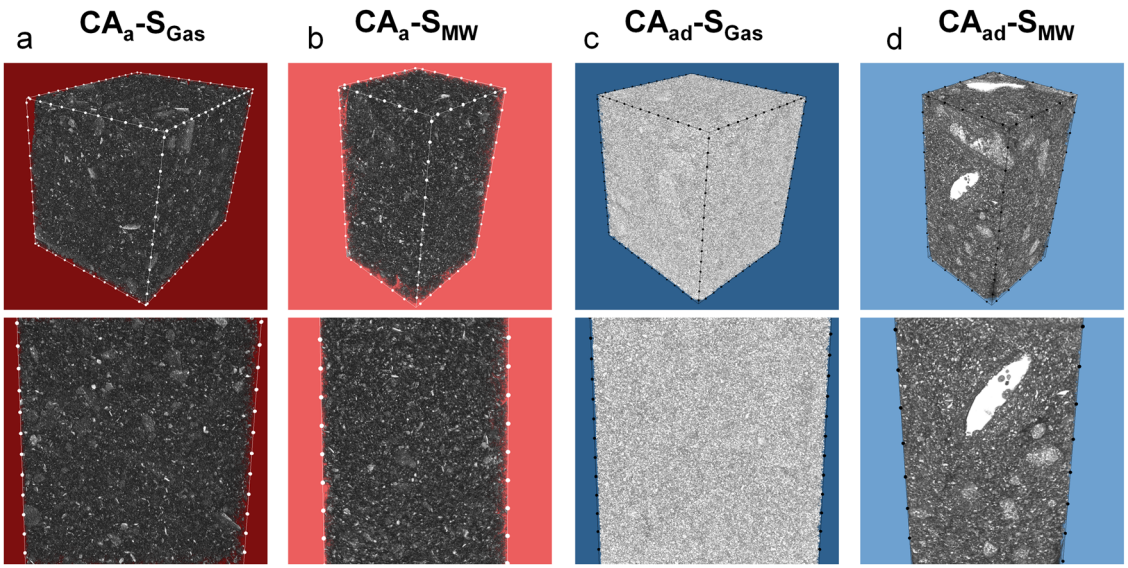

Fig. 4 Reconstructed 3D images of the analyzed carbon sulfur aerogels (a) CA_a–S_{Gas}; (b) CA_a–S_{MW}; (c) CA_{ad}–S_{Gas}; and (d) CA_{ad}–S_{MW} with a selected volume (top row) and a zoom (bottom row). The distance between two circles in the sample frames represents 500 μm. For more 3D images see Fig. S3 in the SI.

sample CA_{ad}–S_{MW} (see Table 3), which supports the assumption of formation of sulfur aggregates or large particles as supposed from CT analysis. Separation of sulfur particles (as seen in CT images, especially for CA_{ad}–S_{MW}) are not observed in following SEM images. This does not exclude the fact that they are existing, as it might be a coincidence that the simple regions analyzed by SEM were all relatively homogeneous, see Fig. 5. On the other hand, CT is not a qualitative technique and it is possible (but not very likely) that the observed particles (specially for CA_{ad}–S_{MW}) are not sulfur based.

From the shown CT analysis, it seems that success of sulfur infiltration depends on both the used carbon aerogel but also the infiltration method.

SEM images in Fig. 5 (top row) reveal comparable morphology of the two carbon sulfur aerogels CA_a–S and CA_{ad}–S independent of the sulfur infiltration method. For CA_{ad} edge-

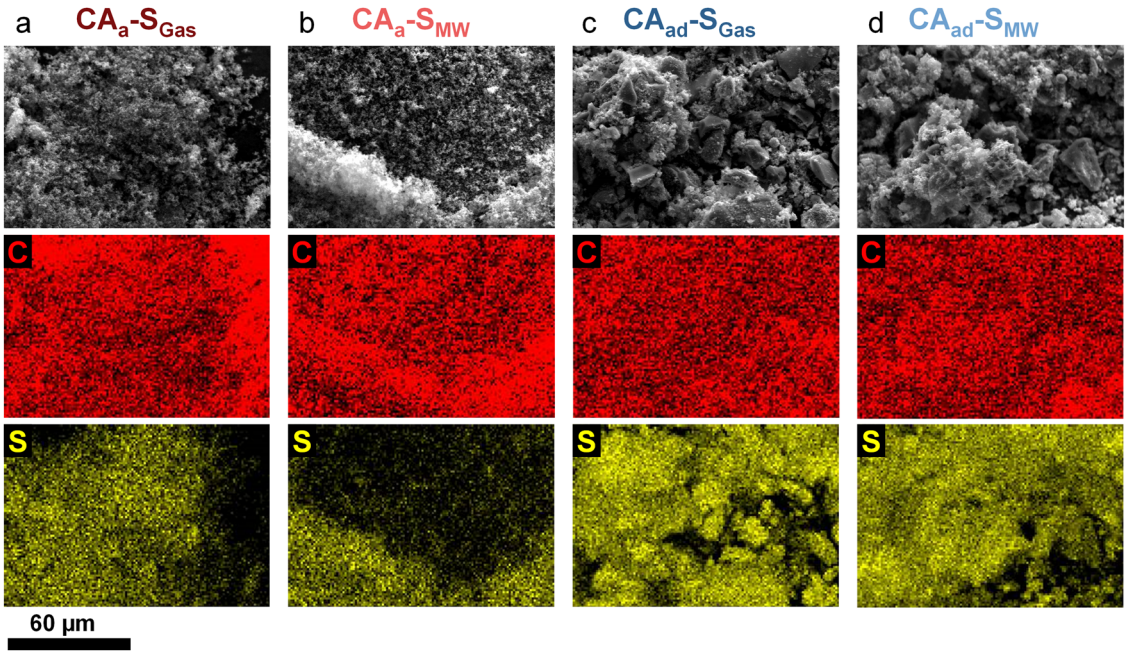

Fig. 5 SEM images and elemental mappings of carbon (C, red) and sulfur (S, yellow) of the analyzed aerogels: (a) CA_a–S_{Gas}; (b) CA_a–S_{MW}; (c) CA_{ad}–S_{Gas}; and (d) CA_{ad}–S_{MW}.

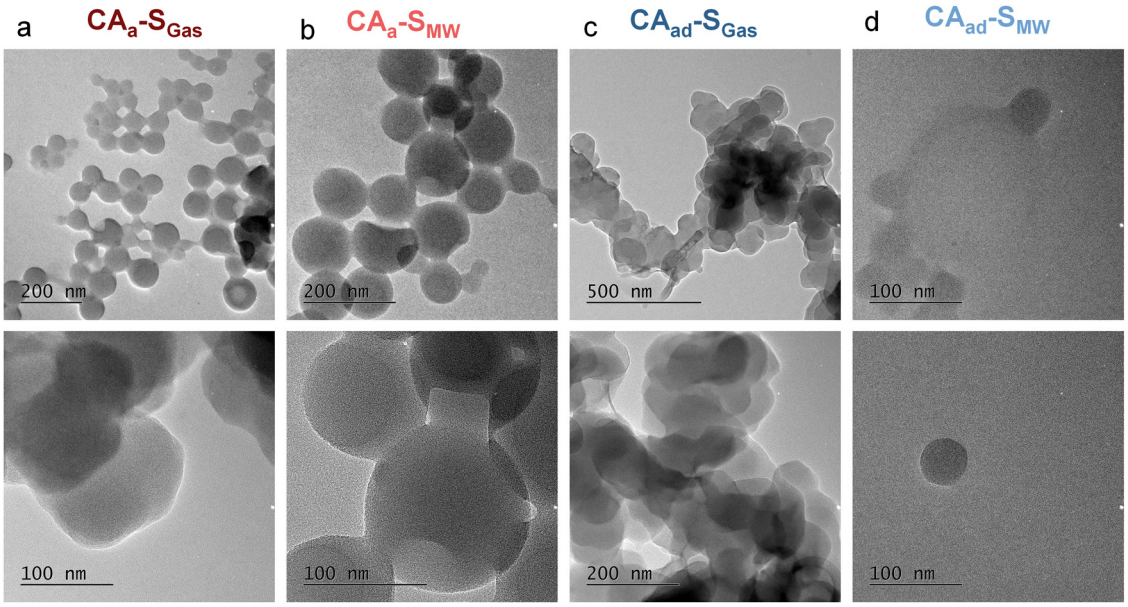

Fig. 6 TEM images of the analyzed aerogels in lower magnification (top row) and higher magnification (bottom row): (a) CA_a–S_{Gas}; (b) CA_a–S_{MW}; (c) CA_{ad}–S_{Gas}; and (d) CA_{ad}–S_{MW}.

shape particles in some parts of the sample can be observed (Fig. 5c and d). The elemental distribution as presented in the middle and bottom row of Fig. 5 shows a quite homogeneous sulfur distribution for all samples. On this scale of the samples, the different infiltration methods seem not to result in severe separation of the elements. The carbon mapping is not representative here due to carbon tape for attachment of the sample on the holder. In comparison to the discussed results from μ-CT analysis, the elemental separation in case of CA_{ad}–S_{MW} (Fig. 4d) is not observed from the SEM images.

Acquisition of TEM images appeared to be quite challenging due to the low density of the mostly C- and S-containing samples which resulted in low stability of the sample under the electron beam. Nevertheless, Fig. 6 reveals that all samples consist of spherical particles with size of approximately 100 nm. No differences between the samples based on the infiltration method can be observed.

In summary, the sample analysis shows that both methods are well suited for sulfur infiltration of porous carbon. The sulfur amount, as well as sulfur loading is predominantly in micropores in gas phase infiltrated samples. Covalently bonded sulfur could be proven by XPS analysis. However, μ-CT gives highly valuable insights on macroscale level. For microwave infiltration some inhomogeneities as well as large sulfur aggregates could be observed. These particles are undesired for *e.g.* metal–sulfur batteries due to the rapid loss of active material (sulfur) during first cycles.[65] The reason for the formation of agglomerates may be the inhomogeneous heat distribution in the material. Possibly, the sample is irradiated inhomogeneously with microwaves, so that sulfur infiltration is not equally effective at all points in the sample. This fact should be taken into account for upscaling experiments. The microwave irradiation should cover the whole sample volume with the same

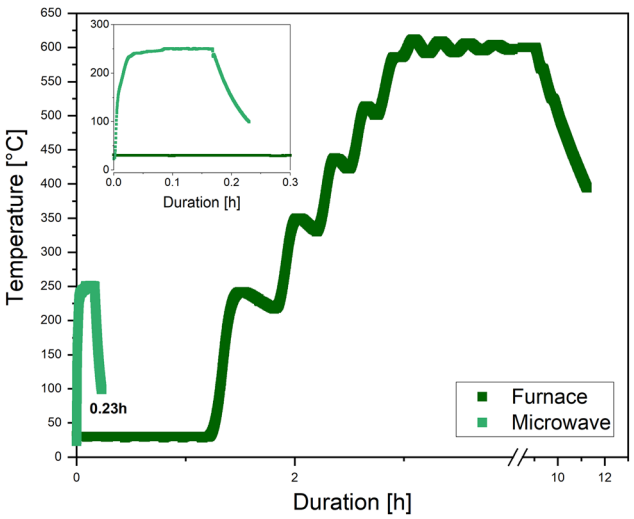

Fig. 7 Temperature-time profile of gas-phase (recorded in inner tags oven) and microwave infiltration (temperature was measured at reactor walls).

power. In contrast, gas-infiltrated samples consist of uniformly distributed sulfur. On the other hand, this technique is highly time-consuming and energy intensive. Fig. 7 depicts the time-temperature profile of both methods. The temperatures given in Fig. 7 were measured for microwave at the microwave reactor wall and during gas-phase infiltration in the inert gas oven. Presumably, the actual sample temperatures will differ from the temperature of reactor walls. In particular, thermal inhomogeneities during microwave treatment cannot be ruled out. The temperature was maintained at 250 °C by adjusting the incident microwave power based on real-time internal temperature measurements. The time–power–temperature plot can be

found in SI (Fig. S4). The microwave infiltration is finished after 0.23 h, whereas the gas-infiltration takes 12 h. From an economic point of view, gas-phase infiltration is a long and expensive method. In addition, the scaling of this method is very difficult to realize: high-pressure stable and sulfur inert vessels are needed to scale up the technique. A distinct big advantage of both methods is that no solvent waste is produced during the infiltration. Additionally, sulfur is distributed only in the pores and not on the particle surface, thus no additional evaporation of surface-sulfur is needed to be performed.

In order to estimate both methods for different applications diverse tests are planned and would be the focus of follow up studies. Since successful filling of micropores could be achieved with the performed techniques it is expectable that electrochemical results in *e.g.* lithium–sulfur battery will show sufficient cycle stability. Moreover, through the formation of the carbon–sulfur bonds the shuttle effect and dissolution of polysulfides are expected to be effectively suppressed, which is already shown in the literature.[58] Additionally, gas-phase mercury capture is expected to be effective due to formation of S–C bonds and infiltration of micropores, where the sorption of Hg is preferable.

Conclusion

To date, the melt infiltration techniques are the most common methods for sulfur infiltration for several applications. This study deals with gas-phase and microwave-based sulfur infiltration and comprehensive characterization of the obtained samples. The microwave infiltration technique was found to be an elegant and simple method to infiltrate micropores of carbon aerogels. Nevertheless, some inhomogeneities, sulfur on the carbon surface and sulfur agglomerates could be observed in the structure. Additionally, the study shows high efficiency (81.1%) of microwave infiltration toward carbon aerogels with large micropores (1–2 nm) and small (2–4 nm) mesopores. In contrast, for carbon aerogel with pores smaller than 1 nm, the technique is ineffective. The gas-phase sulfur infiltration resulted in highly homogeneous sulfur deposition in micropores of carbon aerogels. Although, this technique is time-consuming and energy intensive, the efficiency of micropore loading is about 81–93%. Gas-phase infiltration technique led to an increase in electrical conductivity of carbon aerogels which is beneficial especially for electrochemical application. Both infiltration methods result in formation of C–S bonds within the carbonaceous network. The application of CT-analysis fulfills the study with insides into the macroscopic structure of carbon-sulfur samples.

Author contributions

Conceptualization, J. K., H. N., and S. M.; methodology, J. K. and H. N.; validation, J. K., and H. N.; writing – original draft preparation, S. M.; writing – review and editing, J. K., H. N., S. M., P. W., and B. M.; all authors have read and agreed to the published version of the manuscript.

Conflicts of interest

There are no conflicts to declare.

Data availability

The original data are available from the corresponding author upon reasonable request.

Supplementary information (SI) is available. See DOI: https://doi.org/10.1039/d5ma01315a.

Acknowledgements

The authors acknowledge the contribution of Rebekka Probst for TGA measurements and fruitful discussions, and Peter Mechnich for scientific and technical support with microwave technique. The authors acknowledge the Electron and Light Microscopy Service Unit, Carl von Ossietzky University of Oldenburg, for the use of the imaging facilities (HR-TEM – DFG grant INST 184/106-1 FUGG).

References

1 M. Nojabaee, *et al.*, Ultramicroporous carbon aerogels encapsulating sulfur as the cathode for lithium–sulfur batteries, *J. Mater. Chem. A*, 2021, **9**, 6508–6519.
2 D.-W. Park, *et al.*, A dual mesopore C-aerogel electrode for a high energy density supercapacitor, *Curr. Appl. Phys.*, 2016, **16**(6), 658–664.
3 J. Cheng, *et al.*, Multifunctional carbon aerogels from typha orientalis for applications in adsorption: Hydrogen storage, CO2 capture and VOCs removal, *Energy*, 2023, **263**, 125984.
4 K. Wu, *et al.*, An Iron-Decorated Carbon Aerogel for Rechargeable Flow and Flexible Zn–Air Batteries, *Adv. Mater.*, 2020, **32**(32), 2002292.
5 J. Feng, C. Zhang and J. Feng, Carbon fiber reinforced carbon aerogel composites for thermal insulation prepared by soft reinforcement, *Mater. Lett.*, 2012, **67**(1), 266–268.
6 Y. Yan, *et al.*, Carbon/Sulfur Aerogel with Adequate Mesoporous Channels as Robust Polysulfide Confinement Matrix for Highly Stable Lithium–Sulfur Battery, *Nano Lett.*, 2020, **20**(10), 7662–7669.
7 G. A. K. M. R. Bari, K. Lee and J.-H. Jeong, Integrated Design, Fundamental Insights, and Strategic Engineering of Carbon-Based Materials for Next-Generation Lithium–Sulfur Energy Storage Systems, *Int. J. Energy Res.*, 2025, **2025**(1), 3596594.
8 T. Liu, *et al.*, Superior sulfur infiltration into carbon mesosponge via chemical reaction for enhanced cycling stability in lithium–sulfur batteries, *EES Batteries*, 2025, **1**(3), 640–651.

9 S. Dörfler, *et al.*, Challenges and Key Parameters of Lithium-Sulfur Batteries on Pouch Cell Level, *Joule*, 2020, **4**(3), 539–554.
10 D. J. Tarimo, *et al.*, Performance of Microporous Carbon Cathodes and Impact of Cathode/Solid Electrolyte Interphase Formation Using Carbonate and Ether-Based Electrolytes in Lithium–Sulfur Batteries, *ACS Appl. Energy Mater.*, 2025, **8**(16), 12139–12156.
11 J. A. Korpiel and R. D. Vidic, Effect of Sulfur Impregnation Method on Activated Carbon Uptake of Gas-Phase Mercury, *Environ. Sci. Technol.*, 1997, **31**(8), 2319–2325.
12 W. Liu, R. D. Vidić and T. D. Brown, Optimization of Sulfur Impregnation Protocol for Fixed-Bed Application of Activated Carbon-Based Sorbents for Gas-Phase Mercury Removal, *Environ. Sci. Technol.*, 1998, **32**(4), 531–538.
13 C. W. Purnomo and H. Saputra, Manufacturing of slow and controlled release fertilizer, in *Controlled Release Fertilizers for Sustainable Agriculture*, ed F. B. Lewu, *et al.*, Academic Press, 2021, ch. 6, pp. 95–110.
14 X. Zhao, *et al.*, Sulfur-Modified Coated Slow-Release Fertilizer Based on Castor Oil: Synthesis and a Controlled-Release Model, *ACS Sustainable Chem. Eng.*, 2020, **8**(49), 18044–18053.
15 L. Borchardt, M. Oschatz and S. Kaskel, Carbon Materials for Lithium Sulfur Batteries-Ten Critical Questions, *Chemistry*, 2016, **22**(22), 7324–7351.
16 J. Häcker, *et al.*, Investigation of Magnesium–Sulfur Batteries using Electrochemical Impedance Spectroscopy, *Electrochim. Acta*, 2020, **338**, 135787.
17 T. A. Pascal, *et al.*, Liquid Sulfur Impregnation of Microporous Carbon Accelerated by Nanoscale Interfacial Effects, *Nano Lett.*, 2017, **17**(4), 2517–2523.
18 K. Balakumar and N. Kalaiselvi, High sulfur loaded carbon aerogel cathode for lithium-sulfur batteries, *RSC Adv.*, 2015, **5**(43), 34008–34018.
19 L. S. Shankar, *et al.*, Supercritical carbon dioxide assisted synthesis of ultra-stable sulfur/carbon composite cathodes for Li– S batteries, *Mater. Today Chem.*, 2022, **26**, 101240.
20 M. M. Burkitbayev and F. K. Urakaev, Temperature dependence of sulfur solubility in dimethyl sulfoxide and changes in concentration of supersaturated sulfur solutions at 25 °C, *J. Mol. Liq.*, 2020, **316**, 113886.
21 R. Wang, *et al.*, Measurement and Correlation of the Solubilities of Sulfur S8 in 10 Solvents, *J. Chem. Eng. Data*, 2018, **63**(3), 553–558.
22 G. F. Hawes, C. Punckt and M. A. Pope, Probing Sulfur Deposition onto Carbon Nanomaterials from Aqueous, Elemental Sulfur Sols for Lithium–Sulfur Batteries, *ACS Appl. Mater. Interfaces*, 2021, **13**(27), 31569–31582.
23 F.-l Zhu, *et al.*, Microwave assisted preparation of expanded graphite/sulfur composites as cathodes for Li-S batteries, *New Carbon Mater.*, 2016, **31**(2), 199–204.
24 M. K. Schwan, Jessica; Milow, Barbara, Schwefel-Kohlenstoff-Verbindungen mittels Mikrowellen, DE10 2022 121 579.2, DLR, Editor, 2023, Germany.
25 Y. Chen, *et al.*, A Viewpoint on X-ray Tomography Imaging in Electrocatalysis. ACS, *Catalysis*, 2023, **13**(15), 10010–10025.
26 P. Minnmann, *et al.*, Designing Cathodes and Cathode Active Materials for Solid-State Batteries, *Adv. Energy Mater.*, 2022, **12**(35), 2201425.
27 F. J. Pinar, *et al.*, Long-term Operation of High Temperature Polymer Electrolyte Membrane Fuel Cells with Fuel Composition Switching and Oxygen Enrichment, *Fuel Cells*, 2018, **18**(3), 260–269.
28 M. Rastedt, *et al.* Micro-Computed Tomography Imaging of HT-PEM Fuel Cells Under Contact Pressure Control, *ECS Meeting Abstracts*, 2013. MA2013-02(15), 1318.
29 M. Rastedt, *et al.*, Evaluation of HT-PEM Fuel Cells via Load Cycling at High Current Densities, *ECS Trans.*, 2017, **80**(8), 3.
30 P. Sarkezi-Selsky, *et al.*, Lattice Boltzmann simulation of liquid water transport in gas diffusion layers of proton exchange membrane fuel cells: Parametric studies on capillary hysteresis, *J. Power Sources*, 2022, **535**, 231381.
31 B. Satola, L. Komsiyska and G. Wittstock, Corrosion of Graphite-Polypropylene Current Collectors during Overcharging in Negative and Positive Vanadium Redox Flow Battery Half-Cell Electrolytes, *J. Electrochem. Soc.*, 2018, **165**(5), A963.
32 H. Schmies, *et al.*, Reduction of platinum loading in gas diffusion electrodes for high temperature proton exchange membrane fuel cell application: Characterization and effect on oxygen reduction reaction performance, *J. Power Sources*, 2022, **529**, 231276.
33 M. Spielbauer, *et al.*, Experimental investigation of the failure mechanism of 18650 lithium-ion batteries due to shock and drop, *J. Energy Storage*, 2021, **43**, 103213.
34 I. V. Zenyuk and A. Z. Weber, Understanding Liquid-Water Management in PEFCs Using X-Ray Computed Tomography and Modeling, *ECS Trans.*, 2015, **69**(17), 1253.
35 M. Spielbauer, *et al.*, Experimental investigation of the failure mechanism of 18650 lithium-ion batteries due to shock and drop, *J. Energy Storage*, 2021, **43**, 103213.
36 P. Minnmann, *et al.*, Designing Cathodes and Cathode Active Materials for Solid-State Batteries, *Adv. Energy Mater.*, 2022, **12**, 35.
37 B. Satola, L. Komsiyska and G. Wittstock, Corrosion of Graphite-Polypropylene Current Collectors during Overcharging in Negative and Positive Vanadium Redox Flow Battery Half-Cell Electrolytes, *J. Electrochem. Soc.*, 2018, **165**(5), A963–A969.
38 B. Satola, L. Komsiyska and G. Wittstock, Bulk Aging of Graphite-Polypropylene Current Collectors Induced by Electrochemical Cycling in the Positive Electrolyte of Vanadium Redox Flow Batteries, *J. Electrochem. Soc.*, 2017, **164**(12), A2566–A2572.
39 M. Schwan, R. Tannert and L. Ratke, New soft and spongy resorcinol–formaldehyde aerogels, *J. Supercrit. Fluids*, 2016, **107**, 201–208.
40 M. Sevilla, J. B. Parra and A. B. Fuertes, Assessment of the Role of Micropore Size and N-Doping in CO2 Capture by Porous Carbons, *ACS Appl. Mater. Interfaces*, 2013, **5**(13), 6360–6368.

41 K. Y. Foo and B. H. Hameed, Preparation, characterization and evaluation of adsorptive properties of orange peel based activated carbon via microwave induced K2CO3 activation, *Bioresour. Technol.*, 2012, **104**, 679–686.
42 M. Sevilla, G. A. Ferrero and A. B. Fuertes, Beyond KOH activation for the synthesis of superactivated carbons from hydrochar, *Carbon*, 2017, **114**, 50–58.
43 M. Einert, *et al.*, Nitrogen-Doped Carbon Electrodes: Influence of Microstructure and Nitrogen Configuration on the Electrical Conductivity of Carbonized Polyacrylonitrile and Poly(ionic liquid) Blends, *Macromol. Chem. Phys.*, 2015, **216**(19), 1930–1944.
44 I.-Y. Jeon, H.-J. Noh and J.-B. Baek, Nitrogen-Doped Carbon Nanomaterials: Synthesis, Characteristics and Applications, *Chem. Asian J.*, 2020, **15**(15), 2282–2293.
45 F. Márquez-Montesino, *et al.*, Activated Carbon by Potassium Carbonate Activation from Pine Sawdust (Pinus montezumae Lamb.), *Chem. Eng. Technol.*, 2020, **43**(9), 1716–1725.
46 D. Gu, *et al.*, Facile Synthesis of N-Doped Graphene-Like Carbon Nanoflakes as Efficient and Stable Electrocatalysts for the Oxygen Reduction Reaction, *Nano-Micro Lett.*, 2017, **10**(2), 29.
47 B. Meyer, Elemental sulfur, *Chem. Rev.*, 1976, **76**(3), 367–388.
48 M. Steijns and P. Mars, The adsorption of sulfur by microporous materials, *J. Colloid Interface Sci.*, 1976, **57**(1), 175–180.
49 V. V. Shinkarev, V. B. Fenelonov and G. G. Kuvshinov, Sulfur distribution on the surface of mesoporous nanofibrous carbon, *Carbon*, 2003, **41**(2), 295–302.
50 S. Zheng, *et al.*, In Situ Formed Lithium Sulfide/Microporous Carbon Cathodes for Lithium-Ion Batteries, *ACS Nano*, 2013, **7**(12), 10995–11003.
51 Z. Li, *et al.*, Advanced mechanisms and applications of microwave-assisted synthesis of carbon-based materials: a brief review, *Nanoscale Adv.*, 2025, **7**(2), 419–432.
52 T. Kim, J. Lee and K.-H. Lee, Microwave heating of carbon-based solid materials, *Carbon Lett.*, 2014, **15**(1), 15–24.
53 A. Dubey and C. L. Dube, Microwave processing of carbon-based materials: A review, *Nano-Struct. Nano-Objects*, 2024, **38**, 101136.
54 X. Deng, *et al.*, Insight into the incredible effects of microwave heating: Driving changes in the structure, properties and functions of macromolecular nutrients in novel food, *Front. Nutr.*, 2022, **9**, 941527.
55 Q. Tang, *et al.*, Free-Standing Sulfur/Carbon Nanocomposite Cathodes for Lithium–Sulfur Rechargeable Batteries, *ACS Appl. Nano Mater.*, 2025, **8**(1), 863–870.
56 S. Usuki, *et al.*, Preparation of Micropore-rich High Surface Area Activated Carbon from N-doped Carbon Precursor and its Application to Positive Electrode in Lithium-sulfur Battery, *Electrochemistry*, 2017, **85**(10), 650–655.
57 M. Yang, E. Trizio and M. Parrinello, Structure and polymerization of liquid sulfur across the λ-transition, *Chem. Sci.*, 2024, **15**(9), 3382–3392.
58 H. Ye, Y.-X. Yin and Y.-G. Guo, Insight into the loading temperature of sulfur on sulfur/carbon cathode in lithium-sulfur batteries, *Electrochim. Acta*, 2015, **185**, 62–68.
59 A. M. Darabut, *et al.*, Influence of thermal treatment on the structure and electrical conductivity of thermally expanded graphite, *Adv. Powder Technol.*, 2022, **33**(12), 103884.
60 S. Shaheen Shah, *et al.*, Preparation of Sulfur-doped Carbon for Supercapacitor Applications: A Review, *ChemSusChem*, 2022, **15**(1), e202101282.
61 C. Chi, *et al.*, Balance of sulfur doping content and conductivity of hard carbon anode for high-performance K-ion storage, *Energy Storage Mater.*, 2023, **54**, 668–679.
62 G. Ma, G. Ning and Q. Wei, S-doped carbon materials: Synthesis, properties and applications, *Carbon*, 2022, **195**, 328–340.
63 Q. Wang, *et al.*, Fabrication of Microporous Sulfur-Doped Carbon Microtubes for High-Performance Sodium-Ion Batteries, *ACS Appl. Energy Mater.*, 2018, **1**(11), 6638–6645.
64 D. Muthuraj, *et al.*, Nitrogen and Sulfur Doped Carbon Cloth as Current Collector and Polysulfide Immobilizer for Magnesium-Sulfur Batteries, *ChemElectroChem*, 2019, **6**(3), 684–689.
65 A. Senol Gungor, *et al.*, Understanding Rate and Capacity Limitations in Li–S Batteries Based on Solid-State Sulfur Conversion in Confinement, *ACS Appl. Mater. Interfaces*, 2024, **16**(49), 67651–67661.